Figures

Figure 2: Change in core aspect resulting from the use of water-based mud (EST204) versus oil-based mud (EST 205). Photos taken 10 month after sampling.

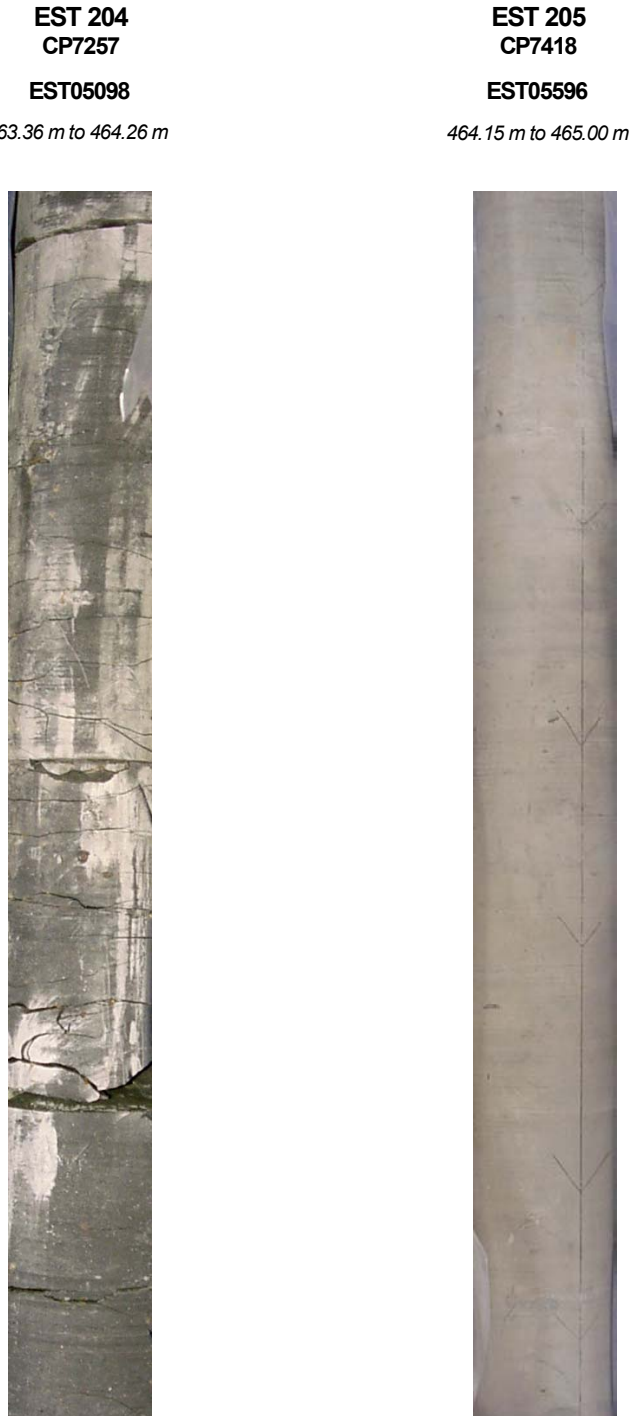

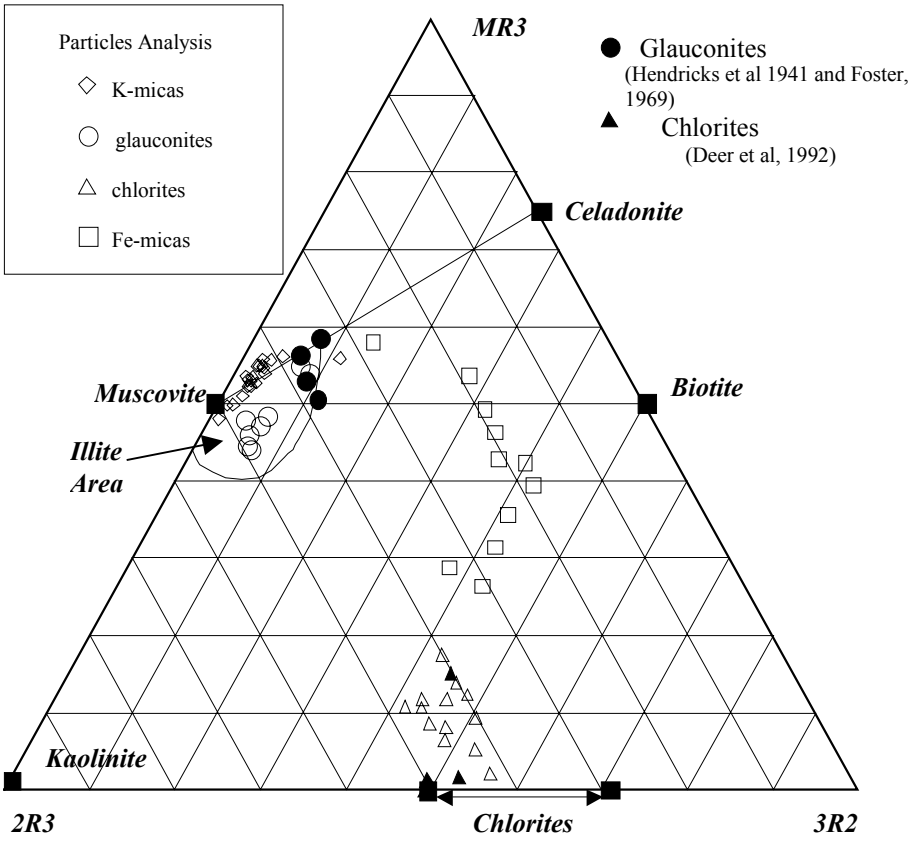

Figure 3: Projection of the phyllosilicate composition analysed by SEM in the system MR^{3+}-$2R^{3+}$-$3R^{2+}$ (Velde, 1985) : $M^{+} = K^{+} + Na^{+} + 2Ca^{2+}$; $MR^{3} = M^{+} - Al^{3+}$; $2R^{3} = [(Al^{3+} + Fe^{3+})-M^{+}]/2$; $3R^{2} = [Fe^{2+} + Mg^{2+} + Mn^{2+}]/3$.

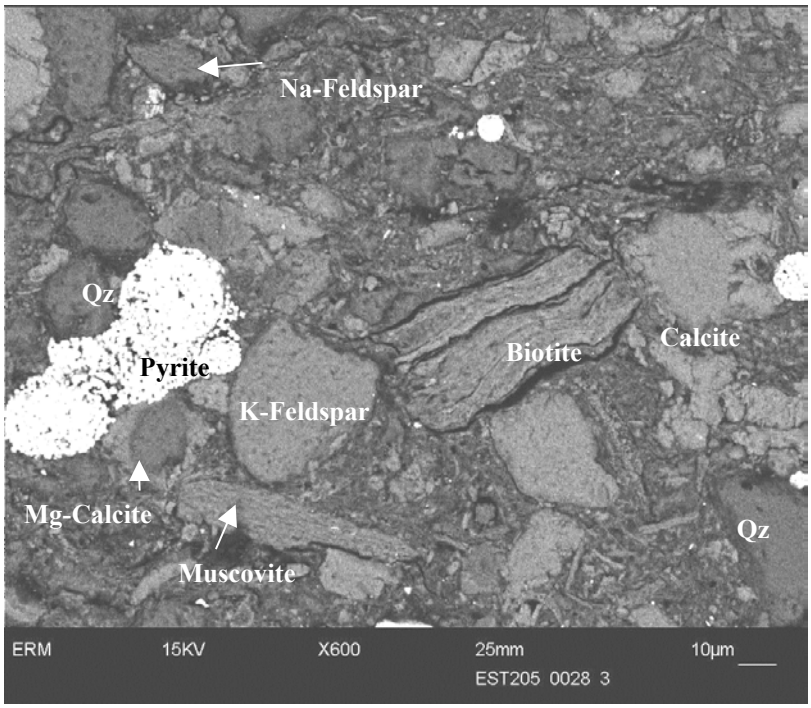

Figure 4: Scanning Electron Micrograph. Sample EST 05460 (429.6 m). Matrix of clays with detrital minerals and pyrite framboïds.

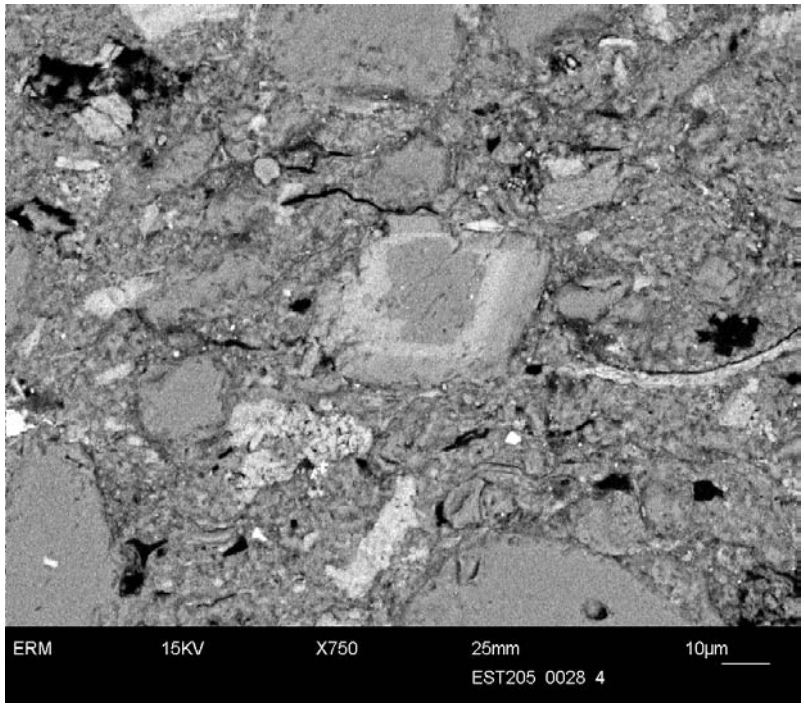

Figure 5: Scanning Electron Micrograph. Sample EST 05474 (432.4 m). Mg-calcite with a variable composition from the centre to the border.

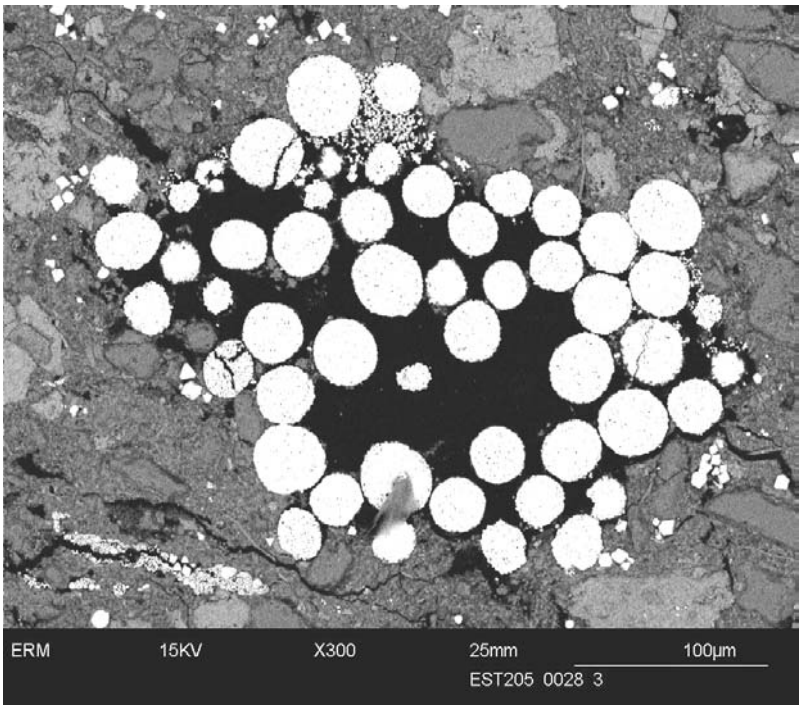

Figure 6: Scanning Electron Micrograph. Sample EST 05505 (442 m). Pyritosphere with organic matter (black).

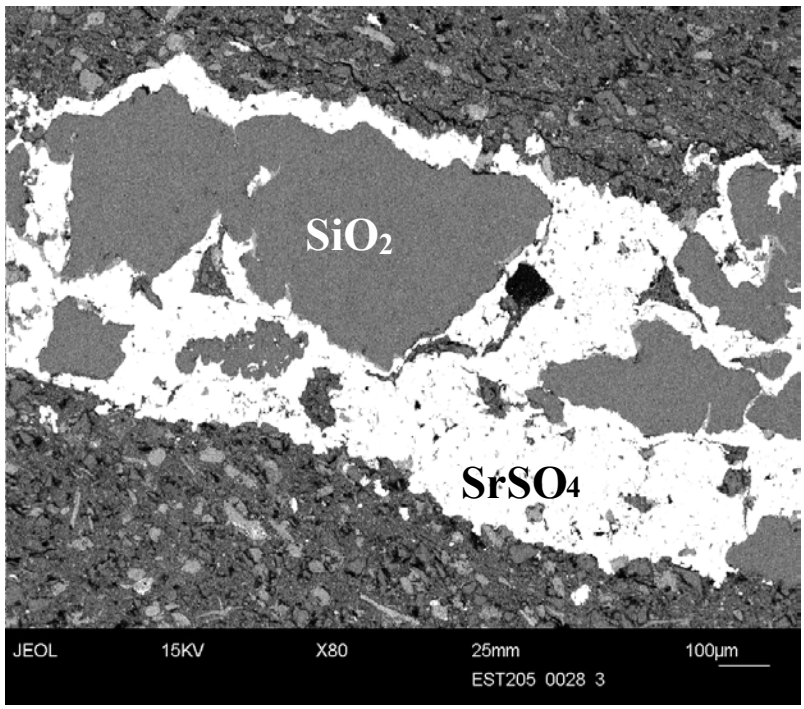

Figure 7: Scanning Electron Micrograph. Sample EST 05632 (475 m). Bioclast filled with celestite and chalcedony (?).

Figure 8 Average mineralogical composition of the different units of the studied interval of the host rock in borehole EST205 and EST103

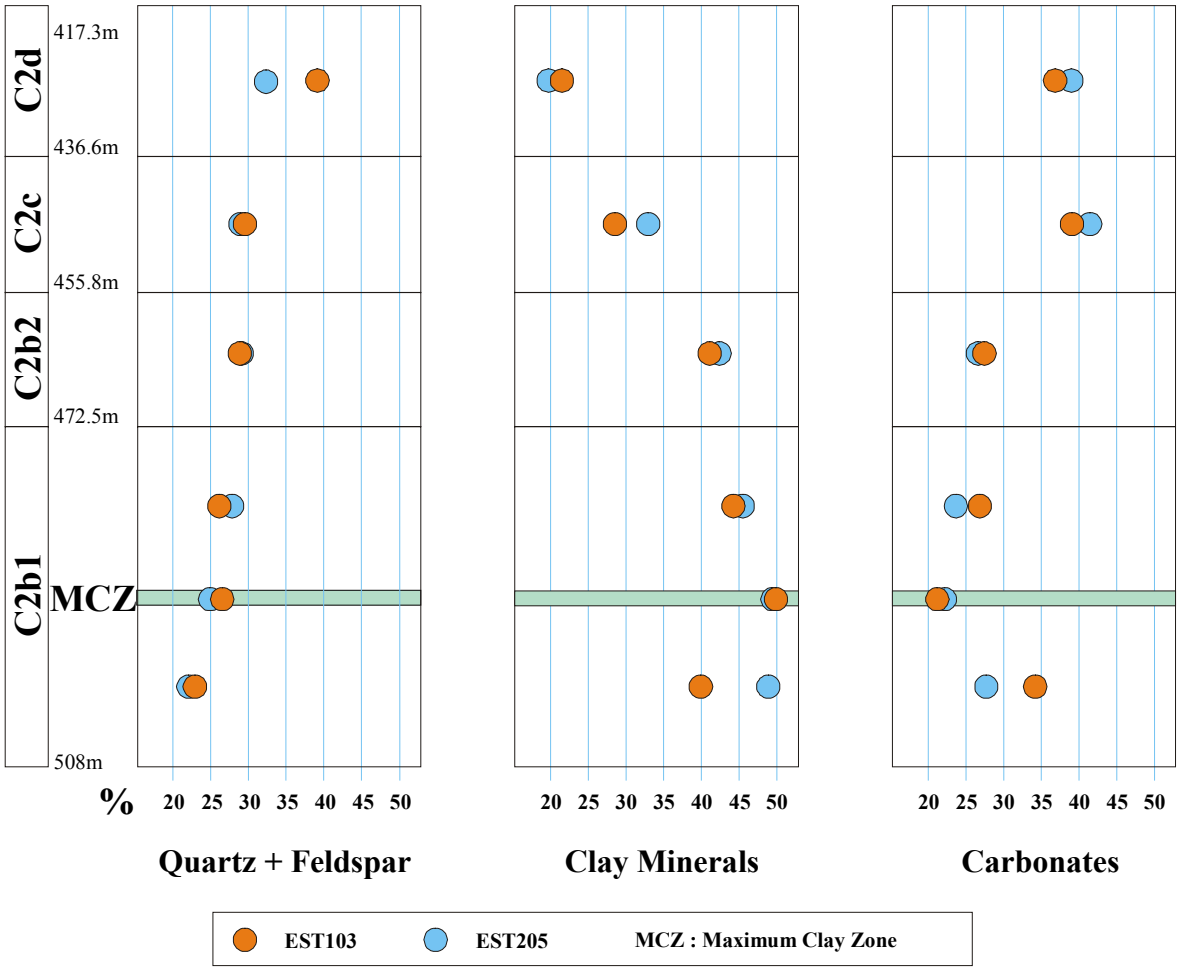

Figure 9: Average grain size composition of the different units of the studied interval of the host rock in borehole EST205 and EST103

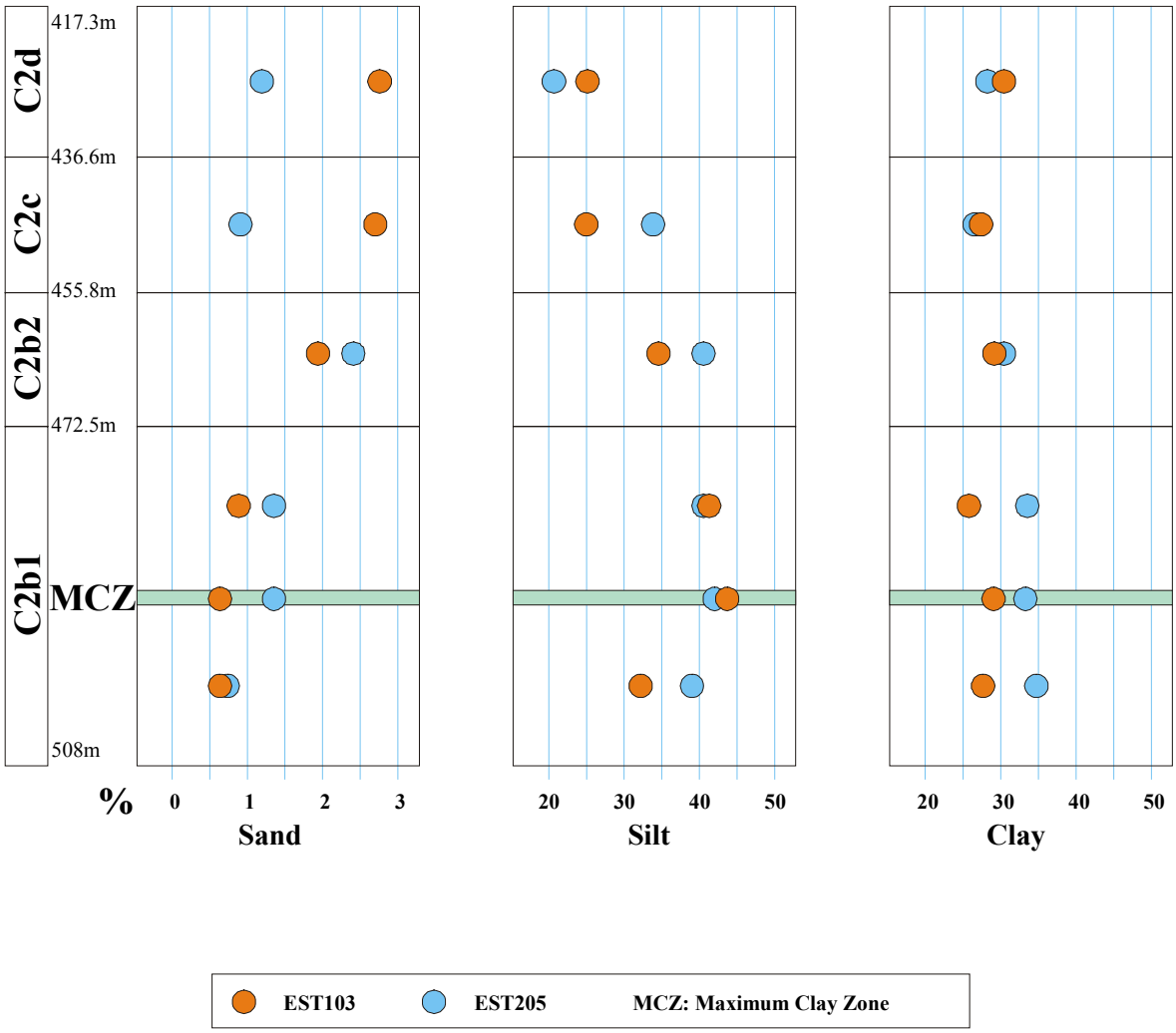

Figure 10: Relationships between mineralogical & particle-size data in the units of the host rock in boreholes EST205 & EST103

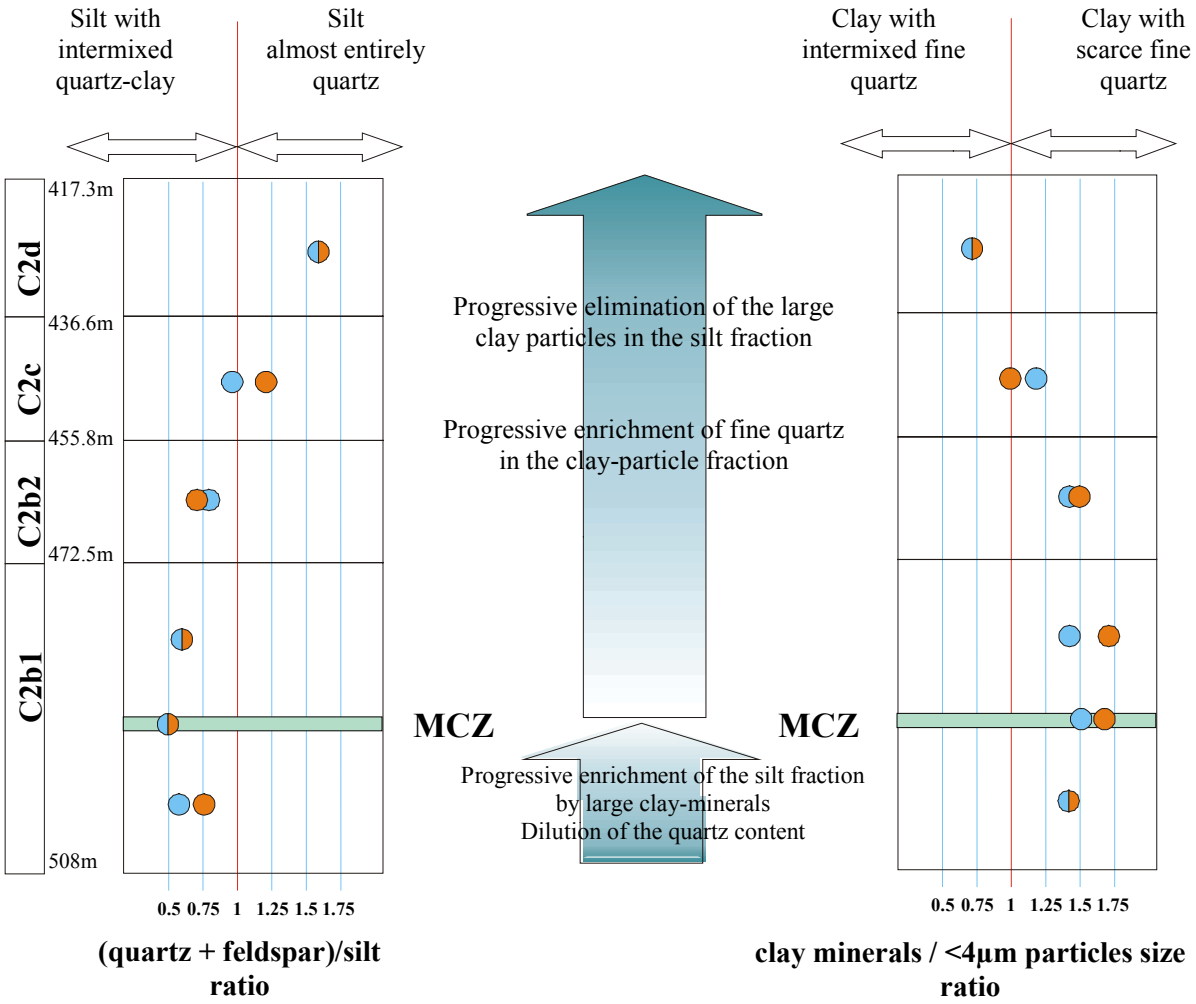

Figure 11: Physical Measurements

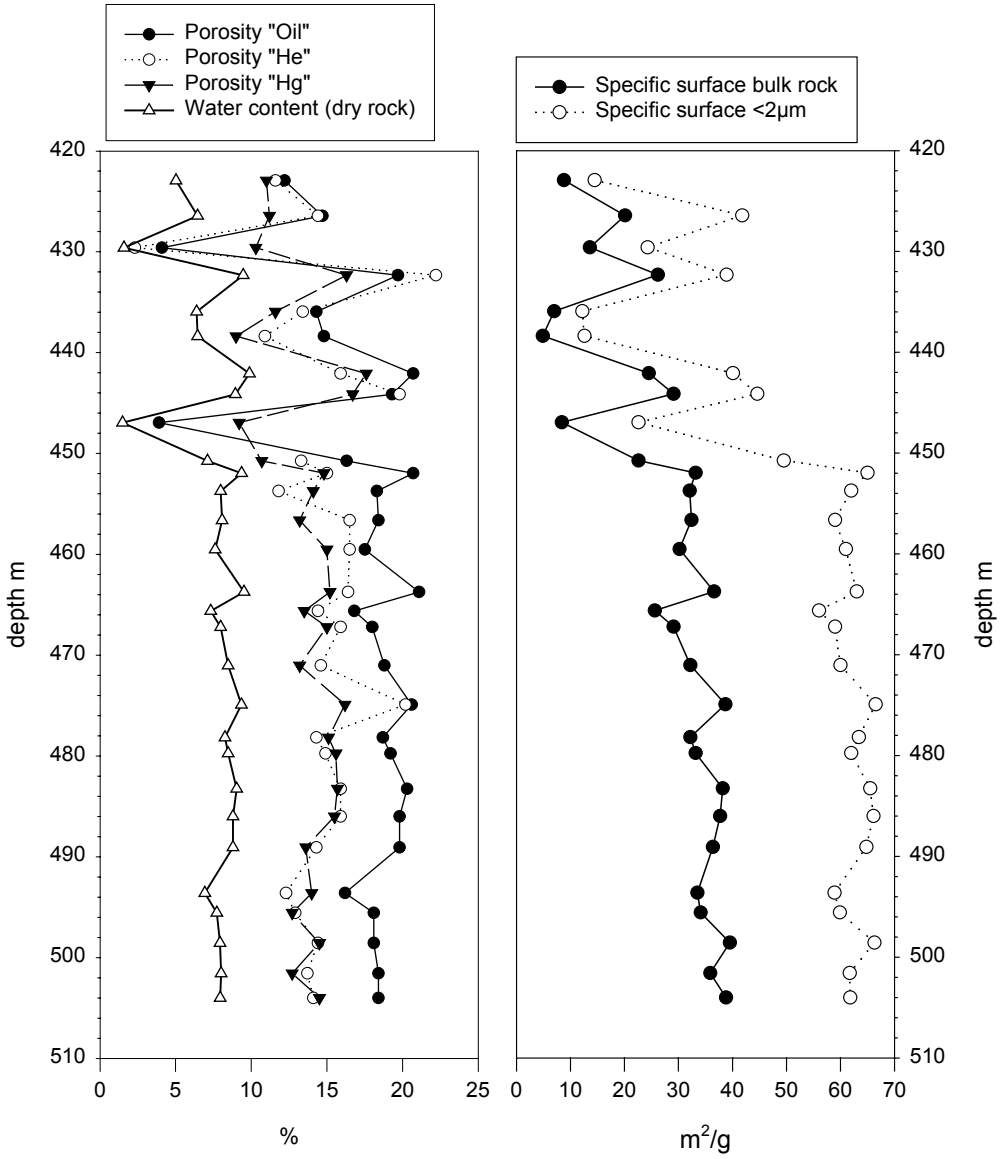

Figure 12: Principal Composant Analysis axes 1 and 2.
Percentage of minerals and elements content

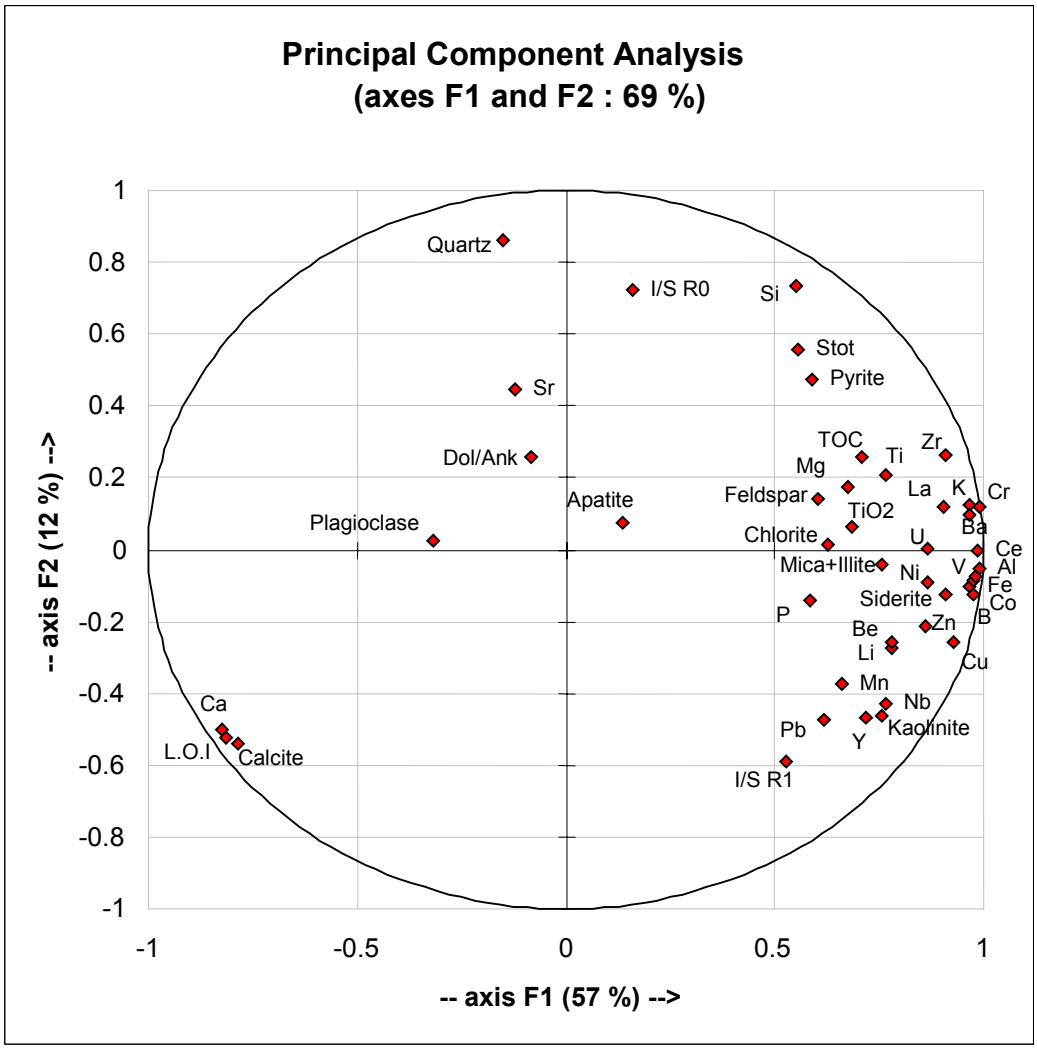

Figure 13: Cl and Br concentration in porewater (total water content, dry rock) and Cl/Br ratio (mg/l).